Electrochemistry-Driven Design of Multiwinding CLLC Resonant Converter

Fabian Groon, *Student Member, IEEE*, Hamzeh Beiranvand, *Member, IEEE*, Dario Metschies, Sergej Schikowski, and Marco Liserre, *Fellow, IEEE*

***Abstract*—The voltage of the lithium-ion batteries is determined by its electrochemistry, which is critical for the optimum design of the connected converter. This, combined with the volume and weight limitations of electric vehicles (EVs), poses a few challenges in terms of increasing the power density and efficiency of the auxiliary power modules (APMs) The APM enables power transfer from the high-voltage traction battery to the low-voltage (LV) loads. Converter efficiency is generally highest at a selected input voltage, while the change in battery voltage is often disregarded when selecting that input voltage. This results in a reduced converter efficiency over the rest of the input voltage range, thereby reducing the potential range of the EV. Therefore, this article proposes a new design approach that considers the electrochemistry of the battery to weight the operation points of the converter and match the input voltage of highest efficiency to the voltage of highest differential capacity of the battery. Hence, the efficiency is better distributed over the entire operating range. Furthermore, a multiwinding CLLC converter with increased peak gain is proposed that distribute the current stress and improve thermal management on the LV side. Experiments verify the new design approach and the proposed converter and an efficiency of 96.6% and power density of 1.36 kW/L including cold plate, microcontroller and protection circuit are achieved.**

***Index Terms*—Auxiliary power module (APM), CLLC, electric vehicle (EV), GaN, multiwinding, planar transformer (PT), resonant converter, topology, battery.**

I. Introduction

THE growth of electric vehicles (EVs) and the demand for more comfort features is bringing dc/dc converters to the spotlight as they require increasingly higher total power, with high efficiency and power density requirements. For this reason, there is an ongoing development from the typical 12 V onboard system to a hybrid 12 V/48 V system or a pure 48 V system [1], [2], [3]. This offers several benefits, as high power can be covered with a 48 V system, lighter cabling is required and higher efficiency can be achieved [1], [4]. The 48 V is primarily used in hybrid systems for high power applications such as active roll stabilization or electric power steering systems [1], [3]. Furthermore, a decentralization of the power in a hybrid system can be realized, thus better managing the power losses [4]. In addition, bidirectional power flow converters offer several advantages over unidirectional converters, as they can be used to support the startup of hybrid vehicles or as an emergency backup [3]. Although improvements have been achieved the effect of electrochemistry in the battery is mainly neglected.

The onboard loads and the electric drive are powered by a high-voltage (HV) battery on the drive system side, with a voltage in the range of 400–800 V [5], [6]. Especially in modern and powerful cars, higher voltages are used on the drive side, which means that in most cases the voltage is above >600 V [5], [7]. This offers advantages and disadvantages, as higher voltage can improve losses by reducing currents, but on the other hand limits the maximum frequency and therefore the power density, since commercially available GaN semiconductors are limited to a blocking voltage of 650 V [8], [9]. In the literature, a method to overcome these limitations has already been proposed in [10]. It solves the issue by connected half-bridges in series to evenly distribute the voltage drop across them, effectively addressing the issue of low blocking voltage in GaN semiconductors. Making it possible to increase voltage levels and utilizing GaN semiconductors for higher power density.

A further way of increasing efficiency and power density is to adopt a multiport topology with a multiwinding transformer. This allows for the coupling of multiple sources or loads to a single transformer and control of the power flow between them [11]. Increased efficiency and power density is achieved as only one transformer and one input stage are required. It can improve the integration of power conversion, thermal management, control, and efficiency [12]. Many multiport topologies have been proposed in the literature [12], [13], [14], [15], which can be adapted or rearranged to obtain new topologies that can be advantageous for some applications. The multiwinding transformer also has advantages in distributing the current stress of the switches compared to paralleling semiconductors. When semiconductors are connected in parallel, current sharing problems arise due to different threshold voltages and different ON-state resistances [16]. Furthermore, it can be observed that

Received 16 December 2024; revised 14 March 2025 and 20 May 2025; accepted 11 June 2025. Date of publication 26 June 2025; date of current version 27 August 2025. This work was supported by the Zentrale Innovationsprogramm Mittelstand (ZIM), which is a funding program of the Federal Ministry for Economic Affairs and Climate Action in Germany under Grant KK5302202PR1. Recommended for publication by Associate Editor X. Pei. *(Corresponding author: Fabian Groon.)*

Fabian Groon and Hamzeh Beiranvand are with the Faculty of Engineering, Kiel University, 24143 Kiel, Germany (e-mail: fagr@tf.uni-kiel.de; hab@tf.uni-kiel.de).

Dario Metschies and Sergej Schikowski are with the Reese Techware GmbH, 25524 Itzehoe, Germany (e-mail: dario.metschies@rxt.de; sergej.schikowski@rxt.de).

Marco Liserre is with the Fraunhofer-Institut für Siliziumtechnologie ISIT, 25524 Itzehoe, Germany (e-mail: ml@tf.uni-kiel.de).

Color versions of one or more figures in this article are available at https://doi.org/10.1109/TPEL.2025.3583480.

Digital Object Identifier 10.1109/TPEL.2025.3583480

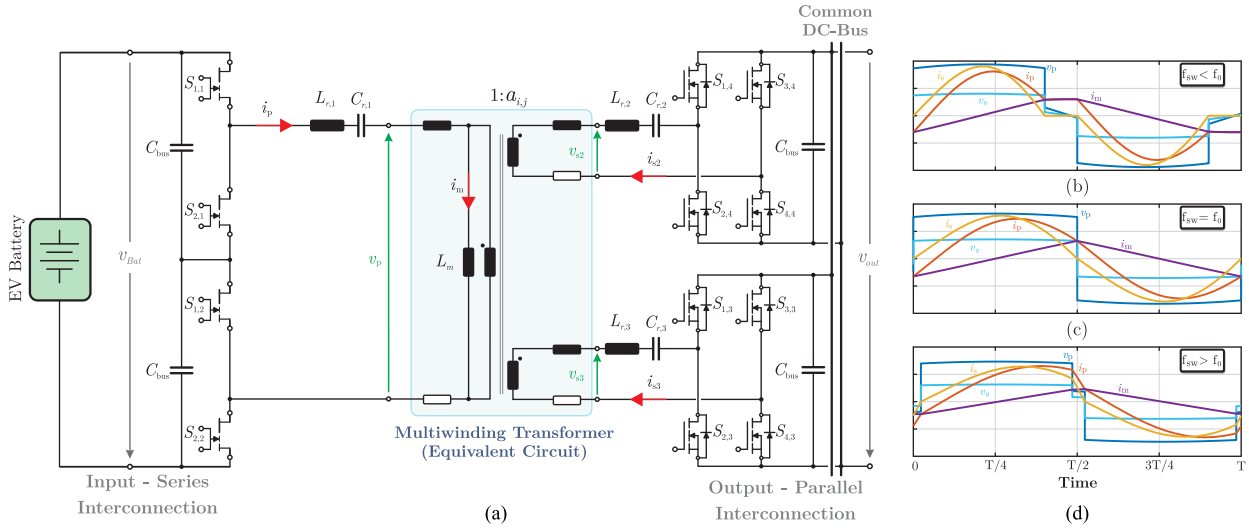

Fig. 1. Electrochemistry effect on the operation of the multiwinding CLLC converter. (a) Proposed multiwinding CLLC topology for APM with distributed voltage and current stress and (b) characteristic operating waveforms of the CLLC converter for switching frequency below resonance frequency, (c) at resonance frequency, and (d) above resonance frequency.

the stray inductance can be reduced by connecting the bridges in parallel, resulting in a lower current imbalance during the transient [17].

The state-of-the-art APM focus on the widely used voltage range from voltage up to 400 V down to 12 V with unidirectional power flow featuring nonresonant (DAB and TAB) and resonant (LLC and CLLC) converters [1], [3], [18], [19], [20], [21]. Most of them following the structure of two-winding transformers, with only a few employing multiwinding transformers [1], [3], [19]. They achieve efficiencies and power densities of around 95% and 1 kW/L [1], [3], [19]. While there is a substantial number of converters in the existing literature for this voltage range, there is only a very limited selection for the upcoming voltage range of >600 to 48 V.

Furthermore, most of the converters in this voltage range are optimized for only one input voltage which, typically is the maximum or minimum input voltage, where the selection of the input voltage for the optimization was not driven by the electrochemistry and the other voltage levels have a degraded efficiency [22], [23]. In EVs the HV battery discharges overtime resulting in a varying input voltage depending on the state of charge of the battery. This influences the optimal operation point of the converter and has so far not be considered in the design process of the system. In addition general parameter optimization for LLC converters are mainly focused on the rms current [24], [25], [26], which only partially effect the optimal design of the converter.

These aspects motivates this article to propose a new design approach that considers the electrochemistry of the HV battery and to develop a converter that achieves high efficiency and power density for precisely this emerging voltage range, that works bidirectionally, and solves the aforementioned problems. The differential capacity, defined by the chemistry of the battery, describes the change in charge for a change in battery voltage and is used to optimize the efficiency of the converter. Therefore, a novel voltage matching approach is introduced where the peak efficiency of the converter is matched to the voltage of maximum differential capacity. Enabling the highest weighted efficiency over the entire state of charge of the battery. In addition, a theoretical analysis is carried out to correlate the factor of switching frequency to resonance frequency with the losses to determine the peak efficiency of the converter. Furthermore, a new multiwinding CLLC topology with distributed current and voltage stress is introduced, enabling the use of GaN HEMTs and achieving increased efficiency compared to a standard CLLC converter through increased peak gain. The proposed converter exceeds the efficiency and power density of current solutions and offer a more evenly distributed efficiency over the varying input voltage range.

II. Proposed Multiwinding CLLC Converter

This section introduces the proposed multiwinding CLLC converter. A time domain model is derived and the advantages of the multiwinding CLLC converter in terms of voltage and current distribution, as well as peak gain, are highlighted. In addition, the design challenges related to current sharing are examined. Furthermore, the voltage gain for the converter is derived.

A. Structure of the Multiwinding CLLC Converter

The resonant CLLC converter introduced in this article for an APM consists of two half-bridges in series on the HV side, a multiwinding transformer and two full-bridges on the LV side. A series capacitor and inductance is placed in each branch to achieve the CLLC resonant converter behavior, as can be seen in Fig. 1(a). The series connection of two half-bridges with GaN HEMTs was selected over HV SiC MOSFETs as GaN HEMTs enable higher efficiency due to the lower turn-OFF losses, lower deadtime requirement and lower gater driver losses. The topology is a combination of several well-known topologies of ISOS and ISOP converters [12], [13], [14], [15]. However, the combination and particularly the parallel LV side with resonant tank in each branch has not been studied in the literature. The authors already provided deeper investigation into a similar

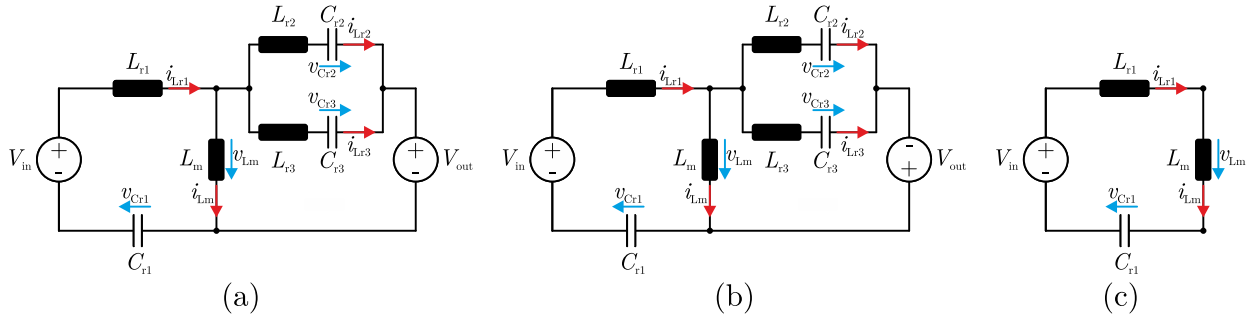

Fig. 2. Multiwinding CLLC resonant equivalent circuits of the first half-cycle during (a) P-stage, (b) N-stage, and (c) O-stage.

topology and parameter deviation of the parallel branches in previous papers [27], [28] as it does not behave like a standard CLLC or parallel LLC converter. The characteristic waveforms of the converter are shown in Fig. 1(b)–(d) and illustrate the square wave voltages across both sides of the transformer and the sinusoidal-like current in the converter branches. Fig. 1(b) shows the converter operating below the resonant frequency. Note that the voltage and current waveforms reach zero before the end of the half cycle and the primary current is equal to the magnetizing current. At the resonant frequency shown in Fig. 1(c) the current is sinusoidal without interruption. Above the resonant frequency, the magnetizing current has not yet reached its peak, but the next half cycle is already starting, interrupting the current flow, as shown in Fig. 1(d). These three operating modes cause each a different loss distribution and therefore a different parameter selection for the optimum efficiency.

B. Analysis of the Design Challenges of the Multiwinding CLLC Converter

A time domain analysis is carried out to demonstrate the advantages and design challenges of the topology compared to the standard CLLC converter. The time domain analysis of the standard CLLC converter is discussed in depth in [29] and [30]. Based on this, the time domain model for the multiwinding CLLC converter is derived. The resonant equivalent circuits for the three stages of the converter are shown in Fig. 2. Given that the LV side is connected in parallel with a multiwinding transformer, the two resonant tanks are also connected in parallel. Therefore, the time domain model for the multiwinding CLLC converter must be extended by two more equations describing the voltage and current relationship between them. The equation system for the P-stage is given in (1) and can also be used for the N-stage, except that V_{out} is negative

$$\begin{cases} V_{\text{in}} = L_{\text{r1}}\frac{di_{\text{Lr1}}(t)}{dt} + v_{\text{Cr1}}(t) + v_{\text{Lm}}(t) \\ i_{\text{Lr1}}(t) = C_{\text{r1}}\frac{dv_{\text{Cr1}}(t)}{dt} \\ i_{\text{Lr2}}(t) = C_{\text{r2}}\frac{dv_{\text{Cr2}}(t)}{dt} \\ i_{\text{Lr3}}(t) = C_{\text{r3}}\frac{dv_{\text{Cr3}}(t)}{dt} \\ i_{\text{Lm}}(t) = i_{\text{Lr1}}(t) - i_{\text{Lr2}}(t) - i_{\text{Lr3}}(t) \\ v_{\text{Lm}}(t) = V_{\text{out}} + L_{\text{rj}}\frac{di_{\text{Lrj}}(t)}{dt} + v_{\text{Crj}}(t), \forall j \in \{2,3\} \\ L_{\text{r2}}\frac{di_{\text{Lr2}}(t)}{dt} + v_{\text{Cr2}}(t) = L_{\text{r3}}\frac{di_{\text{Lr3}}(t)}{dt} + v_{\text{Cr3}}(t). \end{cases} \tag{1}$$

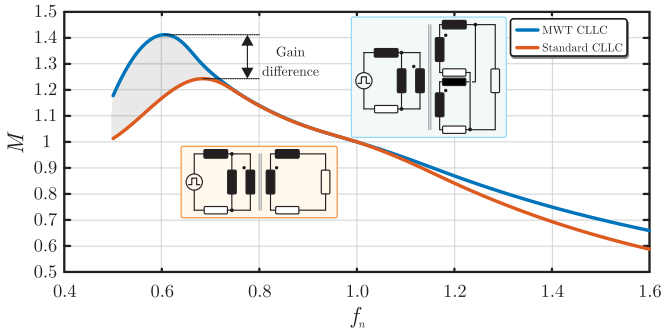

Fig. 3. Gain curve comparison of the proposed multiwinding CLLC converter and the standard CLLC converter for $Q = 0.51$ and $L_{\text{n}} = 5$.

The equation system for the O-stage is given in (2) and is identical to that of the standard CLLC converter, as no power is transferred to the LV side

$$\begin{cases} V_{\text{in}} = L_{\text{r1}}\frac{di_{\text{Lr1}}(t)}{dt} + v_{\text{Cr1}}(t) + v_{\text{Lm}}(t) \\ i_{\text{Lr1}}(t) = C_{\text{r1}}\frac{dv_{\text{Cr1}}(t)}{dt}. \end{cases} \tag{2}$$

These three equation systems can be used to analyze the converters behavior at switching frequencies below, at, and above its resonance frequency. This is achieved by defining the stages that the converter undergoes in a half-cycle, solving the equation system using the Laplace transform, defining the initial conditions, and solving for the variables. Further details of this process can be found in the literature [29] and will not be discussed here, as the process for the multiwinding CLLC converter is similar, except that there are more equations and initial conditions.

Analyzing the multiwinding CLLC converter reveals that it provides a higher peak gain than the standard CLLC converter for the same selected parameters, as shown in Fig. 3. This offers several advantages in terms of the converters voltage range and efficiency, as will be discussed in section IV. Furthermore, if the LV side resonant tanks suffer from a mismatch, it can be seen that there will be a current mismatch. This is due to the different impedances and resonant frequencies of the parallel resonant tanks. This is demonstrated in Fig. 4 through various case studies. When operating below the resonance frequency and there is a mismatch between the LV resonance inductances, it shows that the current sharing between the two ports is unequal, and they operate at different frequencies, as shown in Fig. 4(a) and (b). The difference in current is within a few

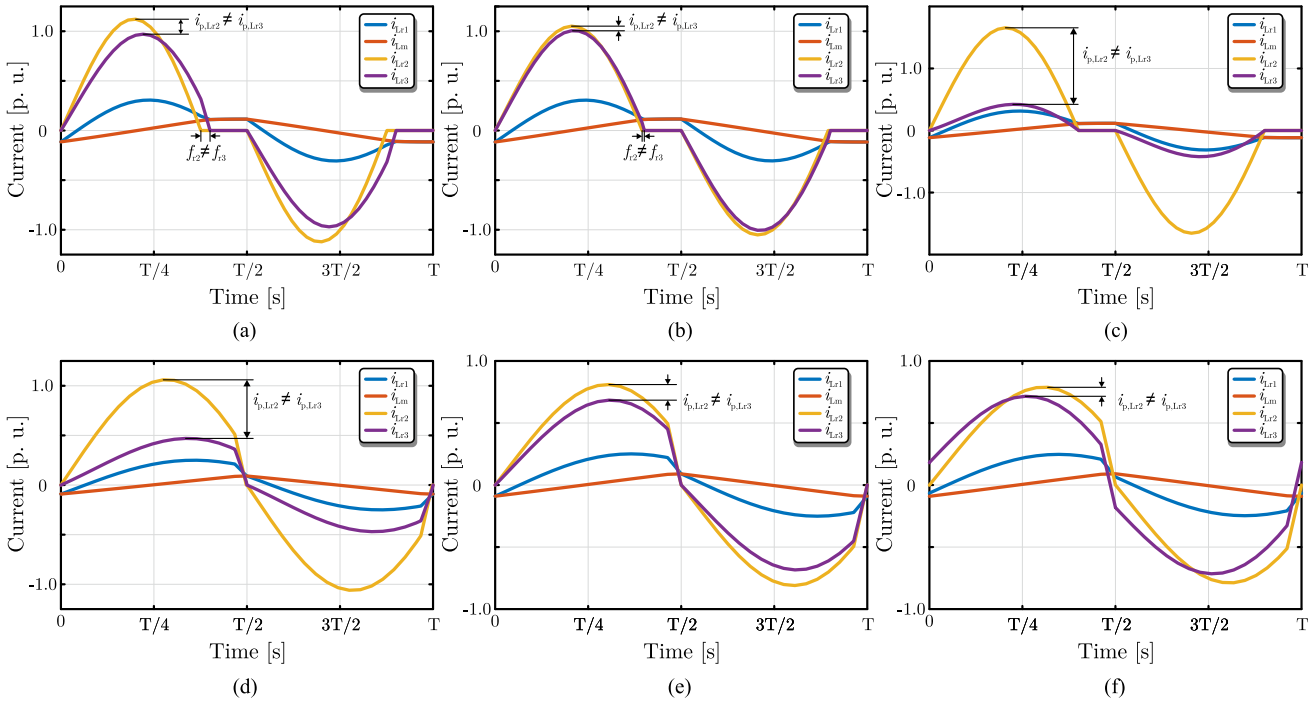

Fig. 4. Simulation results of the influence on current mismatch through parameter deviation at fixed output voltage and power, showing (a) $L_{r2} = 0.8L_{r3}$ at $f_n = 0.8$, (b) $L_{r2} = 0.95L_{r3}$ at $f_n = 0.8$, (c) turns ratio of 7:1.02:1 at $f_n = 0.8$, (d) $L_{r2} = 0.8L_{r3}$ $f_n = 1.2$, (e) $L_{r2} = 0.95L_{r3}$ $f_n = 1.2$, and (f) turns ratio of 7:1.02:1 at $f_n = 1.2$.

percent. However, if the turns ratio is not matched, as shown in Fig. 4(c), the current mismatch is significant and one port processes almost the full power. In the case of an operating point above resonance frequency with a LV inductance mismatch, the current mismatch is significant, as shown in Fig. 4(d) and (e). However, it is less sensitive to a turns ratio mismatch, as shown in Fig. 4(f). Consequently, depending on the operating point of the converter, the current mismatch depends more on the inductance mismatch or the turns ratio mismatch. Therefore, even a small deviation in the inductances or turns ratios can significantly impact the converters performance and should be avoided as much as possible.

C. Simplified Gain of Proposed Multiwinding CLLC Converter

The simplified gain of a resonant converter is described in

$$M(f_{sw}) = \frac{nV_{out}}{V_{in}(Q_b)} \tag{3}$$

where n is the transformer turn ratio, V_{out} the output voltage and V_{in} the input voltage. Since the output voltage is a function of the ac side impedances of the converter, an equivalent circuit is used to derive an analytical equation for the gain. Analyzing this network for the output parallel multiwinding CLLC converter results in the gain equation shown in

$$M_{CLLC,p} = \left| \frac{\frac{X_{Lm}(R_{ac}+X_p)}{X_{Lm}+R_{ac}+X_p} X_{Lzp}}{\frac{X_{Lm}(R_{ac}+X_p)}{X_{Lm}+R_{ac}+X_p} + X_{Lr1} + X_{Cr1}} \right| \tag{4}$$

where R_{ac} is the equivalent ac resistance of the load, X_{Lm} the impedance of the magnetizing inductance, X_p the impedance of the parallel resonant tank on the LV side of L_{r2} and C_{r2}, X_{Lzp} the voltage divider of the impedance of the resonant tank and the equivalent output resistance, and X_{Lr1} and X_{Cr1} the impedance of the HV resonant inductance and resonant capacitor, respectively.

The equivalent ac resistance of the load R_{ac} is calculated by [31]

$$R_{ac} = \frac{8n^2}{\pi^2} R_L \tag{5}$$

with R_L being the load on the output.

There are two key parameters in the resonant converter that influence the gain of the system. These are the loaded quality factor Q of the resonant circuit and the ratio of the magnetization inductance L_m to the resonance inductance L_r

$$Q = \frac{\sqrt{\frac{L_{r1}}{C_{r1}}}}{R_{ac}} \tag{6}$$

$$L_n = \frac{L_m}{L_{r1}} \tag{7}$$

where L_{r1} and C_{r1} are the resonance inductance and resonance capacitance, respectively.

III. Electrochemistry Effects on the CLLC Converter Design

In the following sections, a voltage matching design is introduced that incorporates the electrochemistry of the battery. It is demonstrated theoretically that there is an optimum operating point that can be matched to the battery voltage.

A. Electrochemistry Consideration

The frequency in a resonant converter is directly tied to the input voltage for a fixed output voltage, as can be seen in (3) through the gain. This means that the peak efficiency of the converter can be designed for a specific voltage. This is shown in Fig. 5(a) and (b), where the gain and the efficiency is related to different selected input voltages, respectively. The resonance frequency correlated to the input voltage and therefore the efficiency will vary depending on the voltage selected for the transformer design. The differential capacity ($dQ_{\mathrm{b}}/dV_{\mathrm{bc}}$) for a selected lithium-ion-battery type is shown in Fig. 5(c). It is a measure of the change in capacitance at a specific voltage level in response to a small change in voltage. This means that at peaks with a high change of capacitance, greater energy can be extracted from the battery without a change in voltage. Thus, this differential capacity can be used to weight the operating points of the converter, enabling the optimization of efficiency throughout the converters input voltage range. Furthermore, variation of the resonance tank parameters will also affect the efficiency. Consequently, it is important to weight the operating points, since it is not as straightforward as selecting the parameters with the highest efficiency at the maximum or minimum input voltage.

The total differential charge of the battery ($dQ_{\mathrm{b,total}}$) can be calculated by integrating the voltage dependent charge of the battery over the input voltage range $V_{\mathrm{in,min}}$ and $V_{\mathrm{in,max}}$

$$dQ_{\mathrm{b,total}} = \int_{V_{\mathrm{bc,min}}}^{V_{\mathrm{bc,max}}} dQ_{\mathrm{b}}(V_{\mathrm{bc}})\, dV_{\mathrm{bc}} \tag{8}$$

where V_{bc} is the cell voltage of the battery. By dividing each point of dQ_{b} by $dQ_{\mathrm{b,total}}$ the weighting factor (k_{w}) of each voltage level is obtained

$$k_{\mathrm{w}}(V_{\mathrm{bc}}) = \frac{dQ_{\mathrm{b}}(V_{\mathrm{bc}})}{dQ_{\mathrm{b,total}}}. \tag{9}$$

With N_{bc} in series and V_{bc} of 3.0–4.2 V, the input voltage (V_{in}) range of this converter becomes $N_{\mathrm{bc}}V_{\mathrm{bc}}$. With the calculated losses (P_{Loss}) at each input voltage step and k_{w}, the total weighted losses ($P_{\mathrm{Loss,w}}$) of the converter can be calculated. Making it possible to select the optimal parameters for the entire input voltage range

$$P_{\mathrm{Loss,w}} = \int_{V_{\mathrm{in,min}}}^{V_{\mathrm{in,max}}} P_{\mathrm{Loss}}(V_{\mathrm{in}}) k_{\mathrm{w}}(V_{\mathrm{in}})\, dV_{\mathrm{in}}. \tag{10}$$

B. Optimal Operation Point of the Multiwinding CLLC Converter

In an APM, the converter is connected to a battery on the HV side. This battery defines the minimum and maximum input voltage range of the converter. Based on the number of cells in series (N_{bc}) and the type of battery used, the input voltage range will vary. This input voltage changes depending on the state of charge of the battery and therefore the operating mode of the CLLC converter will change between the modes shown in Fig. 1(b)–(d). This raises the question of which input voltage the converter should be designed for.

To find the point of highest efficiency in a resonant converter the loss equations can be rewritten into a dependency of the gain (M) and the factor of switching frequency (f_{sw}) to resonance frequency (f_0) $f_{\mathrm{n}} = f_{\mathrm{sw}}/f_0$. The transformer has two main losses that occur, the core losses and the winding losses. The core loss density in W/m^3 can be calculated using the Steinmetz equation for a square wave signal [32]

$$P_{\mathrm{v,Core}} = C_{\mathrm{m}} f_{\mathrm{sw}}^{\alpha} B_{\mathrm{max}}^{\beta} \tag{11}$$

where α, β, and C_{m} are the material constants of the selected core. It is apparent that the losses depend on the frequency and the flux density. The flux density can be determined as follows:

$$B_{\mathrm{max}} = \frac{V_{\mathrm{p}}}{4N_{\mathrm{T}} f_{\mathrm{sw}} A_{\mathrm{E}}}. \tag{12}$$

The flux density depends on the input voltage of the transformer V_{p}, the number of windings N_{T}, the frequency f_{sw}, and the size of the core cross-section A_{E}.

Rewriting the flux equations yields

$$B_{\mathrm{max}} = \frac{k_1}{M(f_{\mathrm{n}}f_0) f_{\mathrm{n}} f_0} \tag{13}$$

where k_1 is a constant factor depending on the design of the transformer and the fixed output voltage of the converter. This leads to the core losses equation in dependency of $M(f_{\mathrm{n}}f_0)$ and f_{n}

$$P_{\mathrm{v,Core}} = C_{\mathrm{m}}(f_{\mathrm{n}}f_0)^{\alpha} \left(\frac{k_1}{M(f_{\mathrm{n}}f_0) f_{\mathrm{n}} f_0} \right)^{\beta}. \tag{14}$$

The winding losses can then be calculated based on the ac resistance of the transformer and the rms current of each winding I_i

$$P_{\mathrm{Cu},i} = R_{\mathrm{AC}} I_{\mathrm{i}}^2, \forall i \in \{p, s2, s3\}. \tag{15}$$

For simplicity of the analysis only the primary current is considered. The current on the primary of the converter can be estimated by dividing the operation modes into above and below resonance frequency.

For the above and below resonant mode the current can be approximated by the FHA as long as the converter operates in inductive region

$$I_{\mathrm{rms\_p,above}} = \left| \frac{4nV_{\mathrm{out}}}{\sqrt{2}\pi M(f_{\mathrm{n}}f_0) Z(f_{\mathrm{n}}f_0)} \right| \tag{16}$$

$$I_{\mathrm{rms\_p,below}} = \left| \frac{4nV_{\mathrm{out}}}{\sqrt{2}\pi M(f_{\mathrm{n}}f_0) Z(f_{\mathrm{n}}f_0)} \right| \left(\frac{1}{f_{\mathrm{n}}} - 1 \right) + \left| \frac{4nV_{\mathrm{out}}}{\sqrt{2}\pi M(f_0) Z(f_0)} \right| \tag{17}$$

where $Z(f_{\mathrm{n}}f_0)$ is the impedance of the converter and $(\frac{1}{f_{\mathrm{n}}} - 1)$ is a correction term for the below resonance frequency for the time interval where no power is processed.

The same applies for the conduction losses that are dependent on the ON-resistance ($R_{\mathrm{ds,on}}$) of the device and the current in the converter

$$P_{\mathrm{cond}} = R_{\mathrm{ds(on)}} I^2. \tag{18}$$

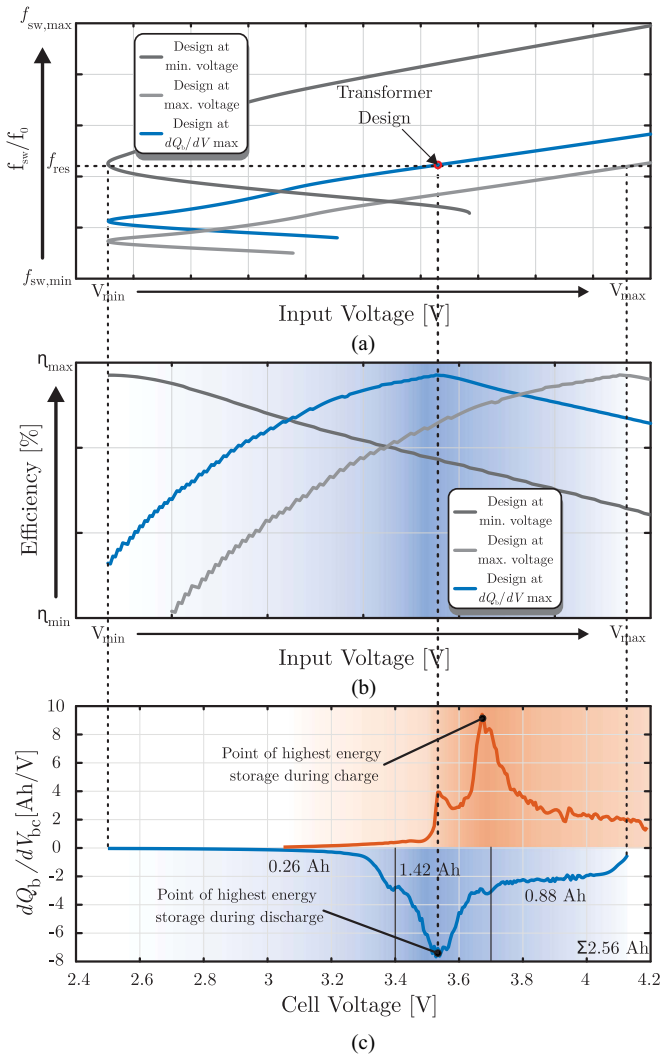

Fig. 5. Influence of the battery on the designing voltage of the converter. (a) Gain correlated to the selected design voltage, (b) efficiency curves for different designs in dependence of the varying input voltage, and (c) available electric charges in dependency of the cell voltage in a lithium-ion battery for charge and discharge.

The switching losses are function of the switching frequency and the switching energy of the device (E_{off})

$$P_{\text{sw}} = E_{\text{off}} f_{\text{sw}} = E_{\text{off}} f_{\text{n}} f_0. \tag{19}$$

Only the switch-OFF losses are considered, as the primary side is switched ON with ZVS and the secondary side is switched ON by rectification. The switching energy changes in dependence of the voltage and current but will be neglected here. The rectification losses are not taken into account as they are typically very low compared to the rest of the losses.

For inductors, the flux density is calculated using the peak current and the inductance value as follows:

$$B_{\text{max,ind},i} = \frac{L_{\text{r}} \hat{I}}{N_{\text{T}} A_{\text{E}}} = k_2 \hat{I} \tag{20}$$

where k_2 is a constant dependent on the selected inductor design.

The total losses of the converter are then simplified as a function of the change in operating frequency only

$$\begin{aligned} P_{\text{total,above}} = C_{\text{m}} & \overbrace{\underbrace{(f_{\text{n}} f_0)^{\alpha}}_{\text{increasing}} \underbrace{\left(\frac{k_1}{M(f_{\text{n}} f_0) f_{\text{n}} f_0}\right)^{\beta}}_{\text{small variation}}}^{\text{increasing}} \\ & + (k_3 + k_4) \underbrace{\left|\frac{1}{M(f_{\text{n}} f_0) Z(f_{\text{n}} f_0)}\right|^2}_{\text{increasing \& small decrease for low } Q \text{ and } L_{\text{n}} \text{ combinations}} \\ & + E_{\text{off}}(f_{\text{n}} f_0) + \underbrace{(f_{\text{n}} f_0)^{\alpha} \left|\frac{k_2}{(M(f_{\text{n}} f_0) Z(f_{\text{n}} f_0))}\right|^{\beta}}_{\text{increasing}} \end{aligned} \tag{21}$$

$$\begin{aligned} P_{\text{total,below}} = C_{\text{m}} & \overbrace{\underbrace{(f_{\text{n}} f_0)^{\alpha}}_{\text{decreasing}} \underbrace{\left(\frac{k_1}{M}(f_{\text{n}} f_0) f_{\text{n}} f_0\right)^{\beta}}_{\text{increasing \& varying for low } Q \text{ and } L_{\text{n}} \text{ combinations}}}^{\text{decreasing}} \\ & + (k_3 + k_4) \underbrace{\left|\frac{1}{M(f_{\text{n}} f_0) Z(f_{\text{n}} f_0)(\frac{1}{f_{\text{n}}} - 1)}\right|^2}_{\text{increasing}} \\ & + E_{\text{off}}(f_{\text{n}} f_0) + \underbrace{(f_{\text{n}} f_0)^{\alpha} \left|\frac{k_2}{M(f_{\text{n}} f_0) Z(f_{\text{n}} f_0)(\frac{1}{f_{\text{n}}} - 1)}\right|^{\beta}}_{\text{increasing}} \end{aligned} \tag{22}$$

where k_3 and k_4 are the resistance values for the semiconductors and the windings of the transformer.

From this analysis it can be seen that the optimum efficiency of the converter will always be at or below resonance frequency. This is due to the fact that all terms for $f_{\text{sw}} > f_0$ increases. Only for a minority of cases, where a small value of Q and L_{n} combinations are used and conduction and inductor losses are dominant this might lead to a small increased efficiency. However, it must be noted, that small values of Q and L_{n} leads to a small impedance Z and therefore the base conduction and inductor losses are already high compared to other solutions. For the case of $f_{\text{sw}} <= f_0$ the switching and core losses decrease and the conduction and inductor losses increase. Therefore, we can conclude that in a high step down converter as used in this article the highest efficiency will be at resonance frequency as the conduction and inductor losses are dominant. Hence, the resonant frequency and input voltage of the transformer should closely match the voltage of the highest dQ_{b}.

IV. Optimal CLLC Converter Design Considering the Electrochemistry of the Battery

The optimization of the converter has to be done in two separate steps. The transformer contributes significantly to the losses of the converter and the individual losses at a given operating point are dependent on the switching frequency. Therefore, the

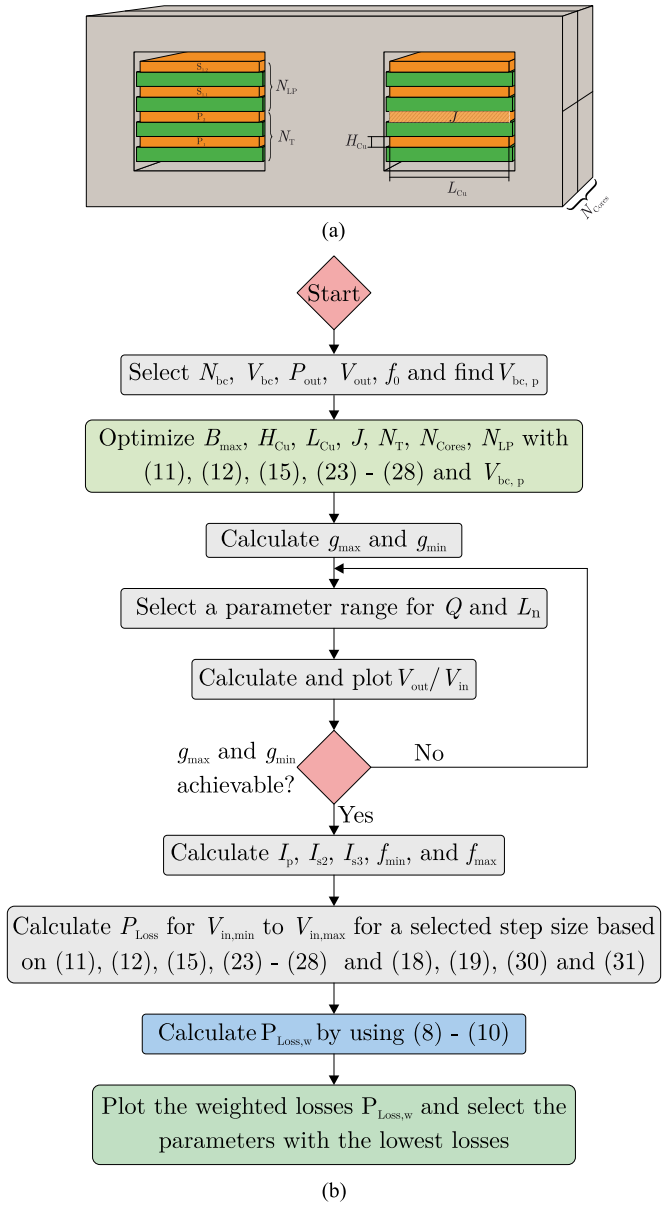

Fig. 6. (a) Geometry of the PT with optimization parameters. (b) Flowchart for the optimization procedure.

design of the transformer should be considered first, as the switching frequency at a given operating point will vary for each combination of resonant tank parameters. Then, the resonant tank parameters should be selected taking into account the losses of the switches, transformer, and inductor. The optimization parameters for the transformer are depicted in Fig. 6(a) and the optimization process is shown in a flowchart in Fig. 6(b).

A. *Optimization of the Multiwinding Planar Transformer (PT)*

For a comprehensive optimization of the PT multiobjective optimization can be considered. This optimization approach has many advantages as it includes the many variables needed for optimization such as the core size, the flux density, the number of cores, the number of windings, the copper thickness and the current density. A $\eta\rho$-pareto optimization is such an multiobjective optimization approach which has been many time showcased in papers [27], [33], [34].

The core losses of the transformer are calculated by (11) and the flux density by (12). The frequency and the input voltage are specified by the application range of the converter and only the number of windings and the size of the core cross-section are available as unconstrained variables for optimization. The input voltage is selected to match the voltage of highest differential capacity of the battery.

The resistance of the windings of the PT can be calculated using the equation from [35]

$$\frac{R_{ac}}{R_{dc}} = \frac{\xi}{2}\left[(H_{ext}-H_{int})^2\frac{\sinh(2\xi)+\sin(2\xi)}{\cosh(2\xi)-\cos(2\xi)} + 2H_{ext}H_{int}\frac{\sinh(\xi)-\sin(\xi)}{\cosh(\xi)+\cos(\xi)}\right] \tag{23}$$

where ξ is the ratio between copper thickness H_{Cu} and skin depth δ and H_{ext} and H_{int} represents the magnetic field strength at the bottom and on top of the layer. The skin depth is fixed by the specified frequency and ξ is therefore only dependent on the copper thickness

$$\xi = \frac{H_{Cu}}{\delta}. \tag{24}$$

The internal and external magnetic fields are calculated based on the current I_i flowing through the winding, the width of one track L_{Cu}, and the number of consecutive layers m [35]

$$H_{int} = (m-1)\frac{I_i}{L_{Cu}}, \forall i \in \{p, s2, s3\} \tag{25}$$

$$H_{ext} = m\frac{I_i}{L_{Cu}}, \forall i \in \{p, s2, s3\}. \tag{26}$$

The dc resistance of each of the winding for PTs can be estimated by

$$R_{DC,i} = \frac{\rho \cdot \mathrm{MLT} \cdot N_{T,i}}{L_{Cu}H_{Cu}}, \forall i \in \{p, s2, s3\} \tag{27}$$

where ρ is the resistivity of copper and MLT the mean length track of one turn. The winding losses can then be calculated based on (15).

The final limitation when optimizing the transformer is the steady-state temperature of the transformer. This is essentially determined by the losses and the volume of the transformer. A simple approximation of the temperature with natural convection can be made as follows [36]:

$$T_{max} = \left(\frac{24}{V_e}\right)^{0.54}(P_{v,Core}V_e + P_{Cu}) + T_A \tag{28}$$

where V_e is the core volume in cm^3 and T_A the ambient temperature, set to 20 °C.

A comprehensive $\eta\rho$-brute-force optimization is carried out to ensure that all relevant parameters are considered simultaneously in the optimization. In this optimization, the parameters J, H_{Cu}, and B_{max} are varied and swept through all possible E-cores available on the market. Note here that for the E-cores even nonplanar cores were considered as a PT design can still

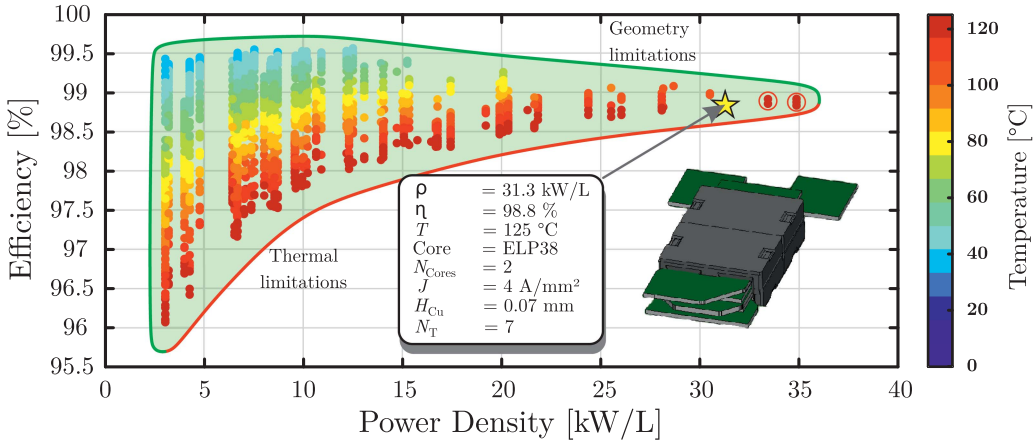

Fig. 7. Pareto front of all available solutions within the acceptable design area for the multiwinding PT.

TABLE I
ELECTRICAL SPECIFICATIONS OF THE CONVERTER

Parameter	
Output power P_{out}	2 kW
Minimum input voltage $V_{\mathrm{in,min}}$	540 V
Maximum input voltage $V_{\mathrm{in,max}}$	760 V
Nominal input voltage $V_{\mathrm{in,nom}}$	650 V
Nominal output voltage $V_{\mathrm{out,nom}}$	48 V
Maximum output voltage $V_{\mathrm{out,max}}$	52 V
Minimum output voltage $V_{\mathrm{out,min}}$	46 V
Nominal switching frequency f_0	250 kHz
Transformer turn ratio	7:1

TABLE II
PARAMETER RANGE OF THE VARIABLES FOR THE $\eta\rho$-OPTIMIZATION

Parameter	Range	Step size
Current density J	2–8 A/mm²	1 A/mm²
Copper thickness H_{Cu}	0.07–0.28 mm	0.035 mm
Flux density B_{max}	0.05–0.3 T	0.05 T

be achieved with nonplanar cores. The specifications of the converter are given in Table I and the parameter range of the optimization is given in Table II. The maximum acceptable temperature is limited to 125 °C. All acceptable solutions are plotted on a graph as a function of power density, efficiency and temperature. The final result of this $\eta\rho$-brute-force optimization is shown in Fig. 7. The adopted design is marked with a star and is located at the upper front of the $\eta\rho$-pareto front. The parameters of the selected design are shown in Fig. 7. The designs highlighted in red circles were not selected because they are conventional rather than planar E-cores and therefore space utilization and final temperature with a cold plate are worse than the selected design.

B. Optimal Parameter Selection for the CLLC Resonant Converter

The efficiency and power density of a resonant converter is influenced by Q and L_{n} shown in (6) and (7), respectively.

Since a CLLC converter has a resonant circuit on both sides of the transformer, it can be designed symmetrically $L_{\mathrm{r1}} = L_{\mathrm{r2}}/n^2, C_{\mathrm{r1}} = n^2 C_{\mathrm{r2}}$ or asymmetrical $L_{\mathrm{r1}} \neq L_{\mathrm{r2}}/n^2, C_{\mathrm{r1}} \neq n^2 C_{\mathrm{r2}}$ [37]. For the optimization in this article, only the case of symmetrical design is considered.

The first step in optimization is to consider the maximum converter gain. The converter must provide sufficient gain of the output voltage to be able to cover the entire required operating range given in Table I. The maximum gain required is obtained from the operating point of 540 to 52 V with a gain of $g_{\mathrm{max}} = 1.348$ and a minimum gain through the operating point from 760 to 46 V of $g_{\mathrm{min}} = 0.847$. The maximum gain of the converter for different values of Q and L_{n} is shown in Fig. 8. It can be observed that the CLLC converter achieves the highest gain at low values for Q and L_{n} and the gain decreases as Q and L_{n} increase. In addition, in Fig. 8 a red line is drawn on the plane which shows the limit of the maximum required gain. All converters with parameter combinations below the line meet the requirement for the maximum gain. All others are unable to achieve the maximum gain. This leads to the first constraint on the parameter selection for the optimum converter design. An additional important feature to consider is that the converter should be able to operate at very low power levels, down to 100 W. Therefore, the converter must be able to reach all the gain points, even in these operating conditions. However, this high load operation is a special case. As can be seen from (6), Q changes with the load. This causes the Q to become very low at high load. Using the equation for the gain of an LLC converter, a formula can be derived that calculates the minimum gain at maximum frequency [38]

$$G_{\mathrm{min},\infty} = \frac{L_{\mathrm{n}}}{L_{\mathrm{n}} + 1}. \tag{29}$$

This minimum gain requirement at low power limits the L_{n} to values below 5.5, as marked in Fig. 8 with another red line.

In addition, the gain limitations for the standard CLLC are mapped onto the gain of the multiwinding CLLC converter. It is noticeable that lower values of Q and L_{n} must be selected to achieve the peak gain.

In the next step, the maximum primary rms current can be considered with respect to both parameters. The rms current

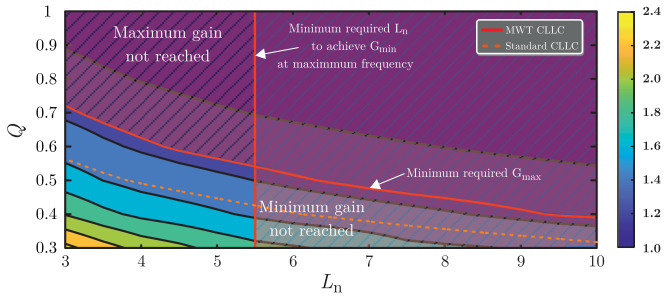

Fig. 8. Maximum attainable gain of the multiwinding CLLC converter for different combinations of Q and L_n and additionally the gain limitation of the standard CLLC converter mapped to the gain curve.

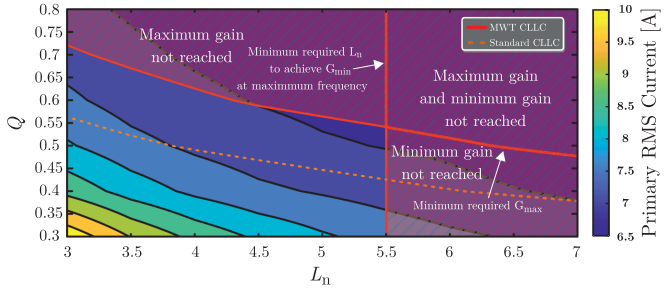

Fig. 9. Maximum primary RMS current at resonance frequency for the multiwinding CLLC and the standard CLLC converter.

has a significant influence on the conduction losses of the semiconductors, the winding losses of the transformer and the inductor losses. The rms current should therefore be as low as possible in order to generate the lowest possible losses. The primary rms current is shown in Fig. 9 for different values of Q and L_n. It is evident that the primary rms current decreases with increasing Q and L_n. Thus, only when considering the primary rms current the largest possible combination of Q and L_n parameters should be selected that still achieves the required maximum gain. When doing so, the largest L_n should be selected first and then the largest Q, as a higher L_n in combination with the Q can achieve a lower current. This results from the fact that a higher L_n reduces the maximum gain less than a higher Q. Compared to the multiwinding CLLC converter the standard CLLC converter requires smaller values for Q and L_n increasing the primary rms current.

Further influence comes from the Q and L_n parameters, which determine the frequency range of the converter required to achieve maximum and minimum gain. A very low frequency, far from the resonance point to obtain the maximum gain, results in very high primary rms currents, which in turn is undesirable, as mentioned previously. Furthermore, the lower the minimum frequency, the higher the core losses of the transformer. A very high frequency, far away from the resonance point, increases the switching losses of the switches, but decreases the core losses of the transformer slightly. In addition, with a wider frequency range, the microcontrollers control effort is greater and small step sizes are difficult to implement. The maximum and minimum frequency to cover all operation points is shown in Fig. 10(a) and (b), respectively. It is apparent that a high L_n

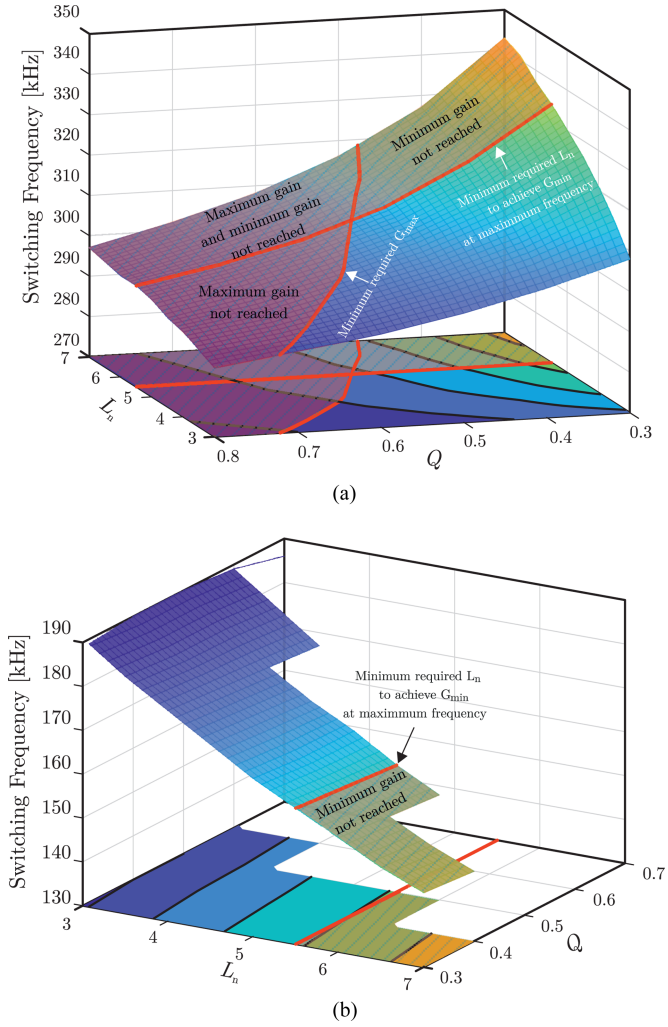

Fig. 10. Switchingfrequency required to achieve all operating points: (a) maximum frequency to achieve lowest required gain and (b) minimum frequency to achieve highest required gain.

and a low Q results in a very high maximum frequency and also a very low minimum frequency. Accordingly, the smallest frequency band can be achieved with a very large Q and a small L_n.

As a final step, the total losses of the converter can be calculated for the individual points of the parameters Q and L_n. For this purpose, the main losses of the converter have to be taken into account. The conduction losses and the switching losses of the semiconductors are calculated by (18) and (19), respectively.

The rectification losses can be approximated as follows [39]:

$$P_{\text{rect}} = 2\sqrt{\frac{V_{\text{th}} V_{\text{g}} V_{\text{F,BD}} V_{\text{F,D1}} I_{\text{out}} C_{\text{g}} f_{\text{sw}} d}{V_{\text{o}}}} \tag{30}$$

where V_{th} is the MOSFET threshold voltage, V_{g} the gate voltage, $V_{\text{F,BD}}$ the body diode voltage drop, $V_{\text{F,D1}}$ the voltage drop of the energy delivery diode, V_{o} the output voltage, d the duty cycle, and C_{g} the input gate capacitance.

The transformer losses can be calculated using (11) and (15). Finally, the core and winding losses of the inductors must be calculated. The flux density of the inductor is calculated by (20).

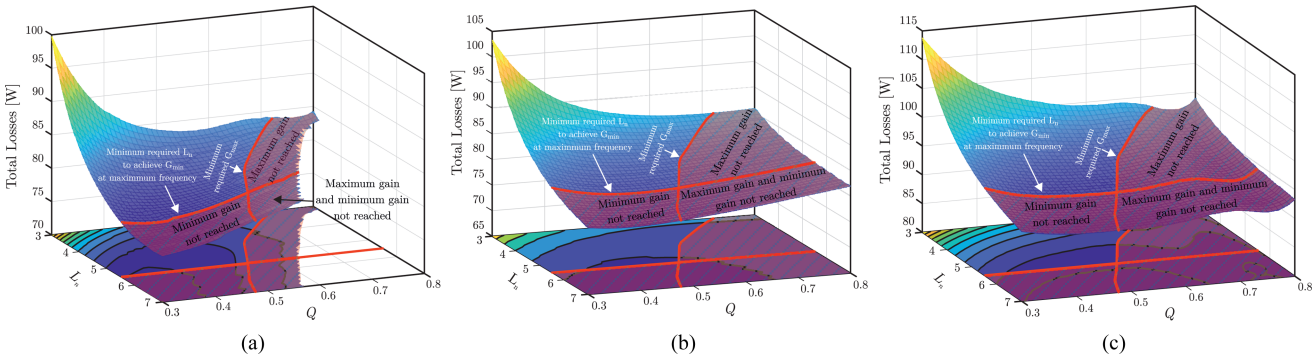

Fig. 11. Total losses of the converter for the different input voltages at (a) 540, (b) 650, and (c) 760 V.

As can be seen, the losses of the inductor depend on the value of the inductance, which is influenced by Q. This makes the optimization process more complex as they are coupled together. To decouple them a simplification is used to calculate the inductor losses. The power of an inductor depends on the size of the inductance and can therefore be calculated as follows:

$$P_{\text{ind},i} = 2\pi f_{\text{sw}} L_{\text{r}} I_i^2, \forall i \in \{p, s2, s3\}. \tag{31}$$

From this power, a fixed efficiency of 99.7% is assumed in order to calculate the losses as a function of the inductor power.

Based on the individual losses, the total losses for the most important operating points can then be determined. For this purpose, the points 540, 650, and 760 V to 48 V are considered. The losses for the individual points of Q and L_{n} at a voltage of 540 to 48 V are plotted in Fig. 11(a). It can be seen that the losses initially decrease with increasing Q and L_{n}, but then increase again in both directions. This is a result of the change in rms current, minimum required frequency and resonance inductance L_{r} as L_{n} and Q are changed.

In Fig. 11(b), the losses are plotted for 650 to 48 V. It can be seen that the losses decrease with increasing L_{n} and Q, but start increasing again with higher values of Q. This is again due to the change in rms current and L_{r}, though this time the minimum frequency is not affected and therefore continuous to decrease with larger L_{n}.

Finally, the losses from 760 to 48 V are shown in Fig. 11(c). A trend similar to Fig. 11(b) can be observed, except that the minimum losses are shifted toward higher Q. Again this is due to the change in rms current and L_{r}.

As illustrated in Fig. 11(a)–(c), the optimal parameter selection for the resonant tank depend on the input voltage of the converter. Therefore, it is important to consider the differential capacity of the battery shown in Fig. 5(c). The individual losses at each voltage step will then be weighted with (8)–(10).

The weighted total losses for different points of Q and L_{n} are plotted in Fig. 12 . As can be seen, the lowest losses occur with a high L_{n} and a low Q. The shape of the curve is similar to Fig. 11(b), as most of the energy can be drawn from the battery at around 3.55 V which is around 639 V input voltage for the converter. Therefore, the highest possible L_{n} with a Q in the range of 0.4–0.55 should be selected for the highest efficiency. Before selecting the parameters, it is also important to note that

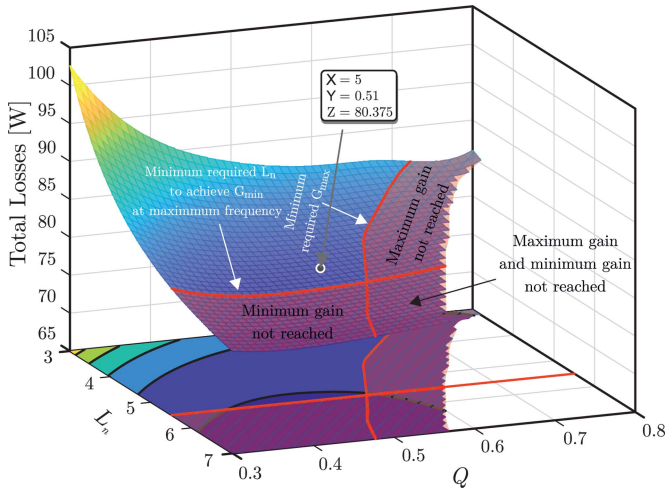

Fig. 12. Weighted losses of the converter according to available energy at different cell voltages in lithium-ion batteries.

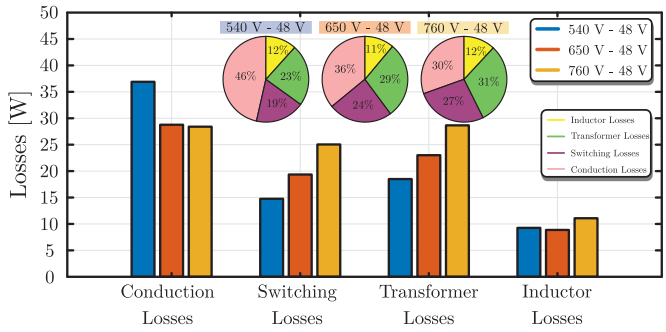

Fig. 13. Loss breakdown at 2 kW output power for the three individual voltages.

the converter must be able to withstand an overload of 110%. As a result, a Q must be selected which, after multiplication by a factor of 1.1, still remains below the marked gain line for maximum gain. The optimum design can then be selected based on these limitations. For this converter, $L_{\text{n}} = 5$ and $Q = 0.51$ were selected. This point fulfills all the requirements and achieves the lowest losses. Based on these parameters, the final inductors design is selected and the losses and efficiency of the system

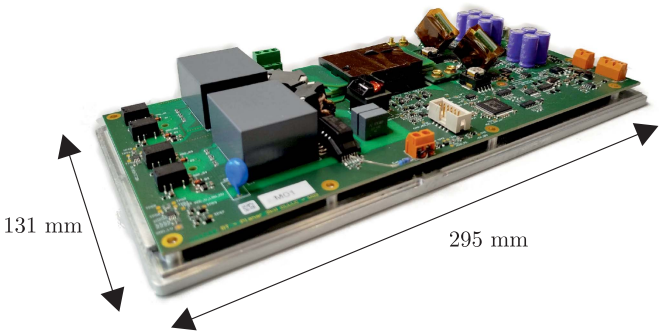

Fig. 14. Prototype of the multiwinding resonant CLLC converter with distributed voltage and current stress including the cold plate (295 mm × 131 mm × 38 mm).

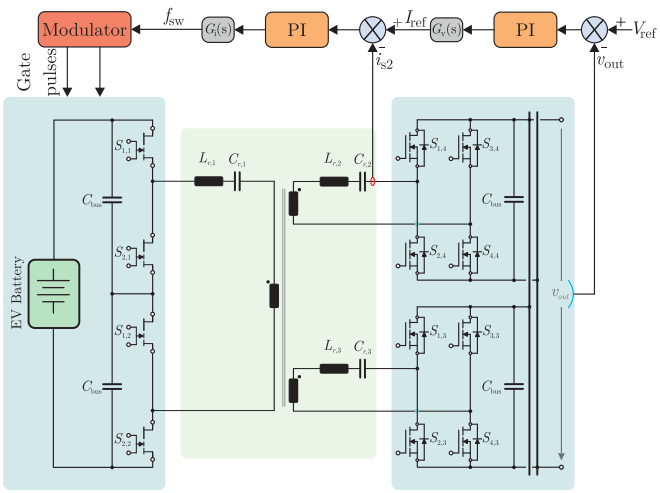

Fig. 15. Simplified control block diagram of the multiwinding CLLC resonant converter.

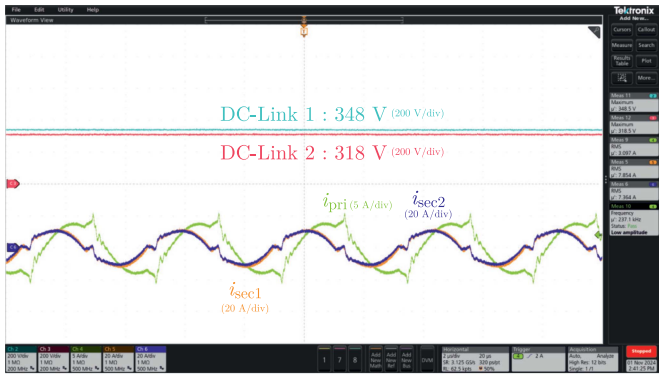

(a)

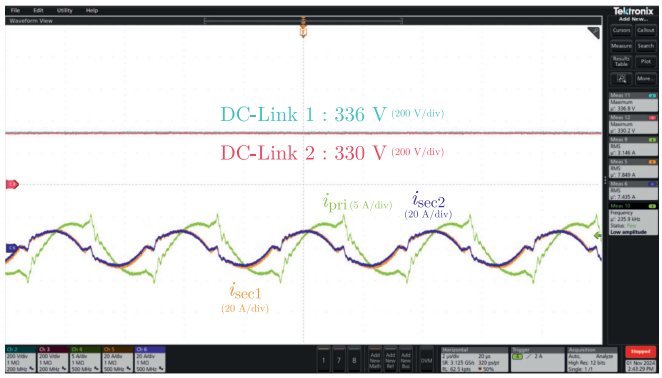

(b)

Fig. 16. DC-link voltages of the series connected half bridge at 650 V and 236 kHz (a) without balancing control and (b) with implemented balancing control.

can be determined. The loss breakdown for the individual input voltages at 2 kW is illustrated in Fig. 13 . The lowest losses occur at 540 and 650 V where an efficiency of 96% is achieved. At 760 V the efficiency is lower as the high switching frequency degrade the efficiency and all losses are increasing or remaining similar. It shows that below 650 V, conduction losses are the main limiting factor, followed by transformer losses.

V. Experimental Results

The multiwinding resonant CLLC converter was built using the parameters obtained from the optimization to validate the benefits of the design approach and the proposed converter topology. The specifications of the converter are listed in Table III. The HV side consists of GS66508T from GaN systems, which offers low ON-resistance, small package size and low switching losses. The LV side employs IPTC014N08NM5 from Infineon, featuring very low ON-resistance, but also low capacitance compared to other solutions, providing a good trade-OFF between low conduction losses and low switching losses in the reverse direction. The auxiliary supply can be provided externally or directly from the LV of the converter.

TABLE III
Electrical Specifications of the Built Converter

Parameter	
HV Mosfets	GS66508T
LV Mosfets	IPTC014N08NM5
Transformer Core	2x ELP38 in Parallel
Magnetizing Inductance	74.3 µH
Primary Inductance, Secondary Inductance	14.8 µH, 303 nH
Primary Capacitance, Secondary Capacitance	27.3 nF, 1.3 µF
Minimum Switching Frequency $f_{sw,min}$	150 kHz
Maximum Switching Frequency $f_{sw,max}$	400 kHz
Power Density	1.36 kW/L

The converter is shown assembled with the cold plate in Fig. 14. In addition, the converter includes a dc-link overvoltage protection circuit and an overcurrent protection circuit for each port, interrupting the PWM signals in case of a fault. A 480 MHz STM32 M7 Cortex controller is implemented to control the PWM signals and monitoring the protection circuits. A closed loop control is implemented to control the output voltage. A simplified block diagram of the control is shown in Fig. 15. The control consists of an outer voltage loop, which controls the output voltage, and an inner current loop, which controls one of the secondary resonance currents. The transfer functions $G_v(s)$ and $G_i(s)$ in between convert the voltage difference into a current reference and the current difference into a frequency,

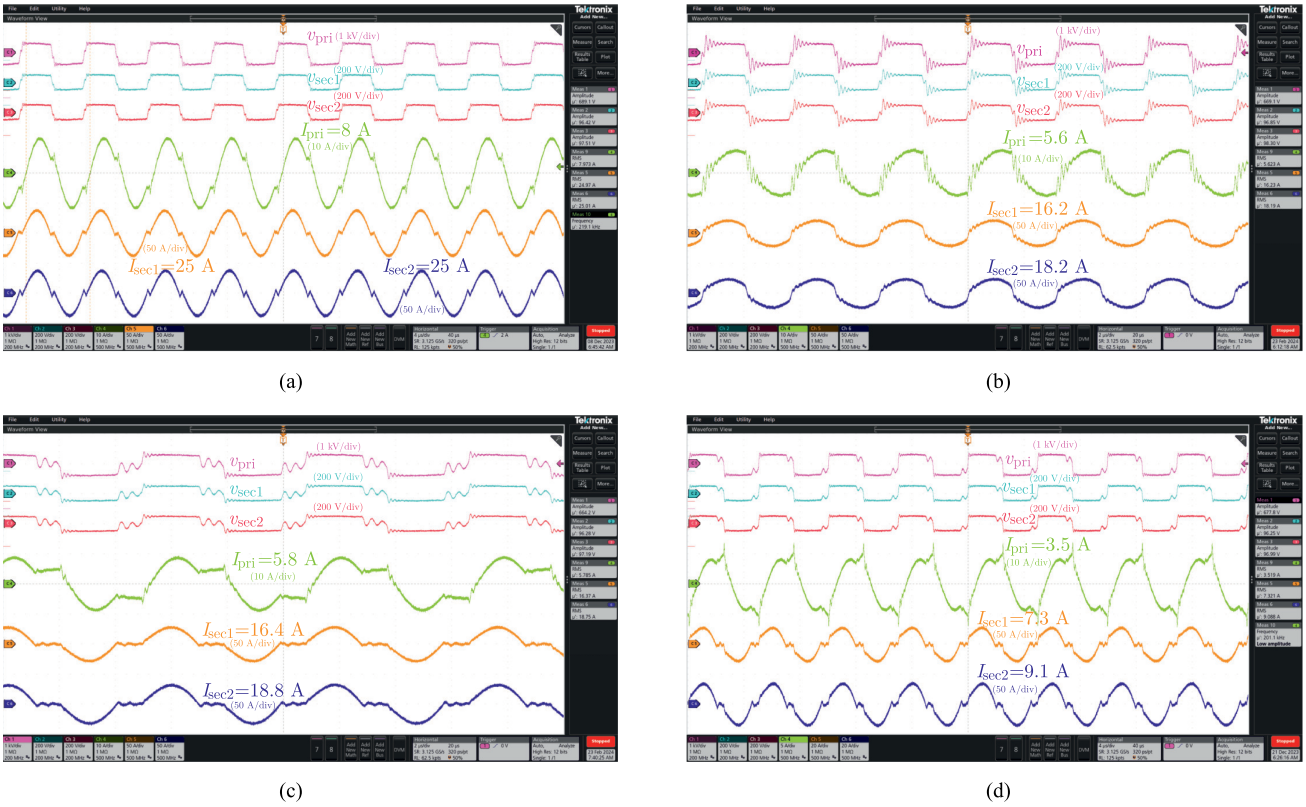

Fig. 17. Waveforms of the prototype at (a) 650 V and 2 kW, (b) 760 V and 1.5 kW, (c) 540 V 1 kW, and (d) 600 V and 620 W.

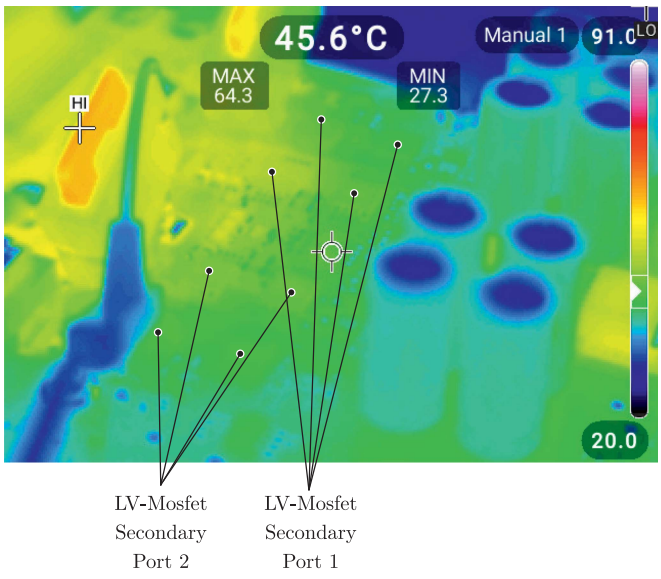

Fig. 18. Thermal profile of the LV switches at 1.5 kW power after 10 min.

respectively. The modulator then sends the pulses at the calculated frequency to the gates of the HV switches. The converter achieves a power density of 1.36 kW/L including the cold plate.

Two distinctive features of the converter are the voltage and current distribution on the semiconductors on the HV and LV sides. The voltage distribution on the HV side and the current distribution on the LV side are essential for the converter to operate above 650 V, reduce the stress on the switches and maximize the efficiency of the system.

The dc link voltages of both half bridges on the HV side for 650 V at 720 W with 236 kHz in closed loop control are shown in Fig. 16(a) for the upper and lower half bridge in yellow and red, respectively. Note that the voltage is distributed between the two half bridges within a deviation of 4%. The voltage distribution depends on the operating point and therefore on the frequency. However, at all operating points there is a maximum deviation of 4% between the dc link voltages. In case a smaller deviation is required, a simple P-controller as proposed in [40] and [41] can be implemented. The dc link voltage with implemented voltage balancing control is shown in Fig. 16(b) and shows that the deviation between the two dc link voltages has been reduced to less than 1%.

The current distribution on the LV side has a significant impact on the efficiency of the overall system, as conduction losses account for the majority of the losses and have a significant impact on the heat distribution of the semiconductors. Various operating points of the converter are shown in Fig. 17. From Fig. 17(a) it can be seen that at 650 V 2 kW the current distribution of the two LV sides is equal and there is no deviation. For input voltages of 540 V at 1 kW and 760 V at 1.5 kW, there is a deviation in the current distribution of 6%, as can be seen in Fig. 17(b) and (c), respectively. This deviation is caused by the fact that the switching frequency is well below or above

TABLE IV
CONVERTER SPECIFICATION COMPARISON

Topology	Input voltage	Output voltage	Power / f_{sw}	Input voltage at peak efficiency and 50 % load	Efficiency variation based on input voltage at 50 % load	Peak efficiency
3p-DAB [42]	100–170 V	10–16 V	2 kW / 100 kHz	140–150 V	87.5 %–95 % @ 14 V	95 %
QSC [43]	300–400 V	12 V	1 kW / 500 kHz	300 V	88 %–92 % @ 12 V	92 %
PSFB with integrated PT [44]	400–800 V	13–15 V	2.1 kW / 200 kHz	400 V	94.5 %–95.2 % @ 14 V	95.4 %
Interleaved LCLC Resonant Converter [22]	250–400 V	12 V	1 kW / 170–280 KHz	400 V	94.8 %–96.4 % @ 12 V	96.7 %
LCLC Resonant Converter [23]	250–400 V	12 V	500 W / 110–250 kHz	400 V	95.4 %–96.1 % @ 12 V	96.4 %
Borgwarner Gen5 [45]	220–800 V	11–13.4 V	1.2 kW / N/A	500 V*	89 %–92 % @ 13.4 V	92 %
Deutronic DVCH1503-400 [46]	200–470 V	2–15 V	1.5 kW / N/A	200 V	92.5 %–95.9 % @ 12 V	96 %
Multiwinding CLLC Resonant Converter (this work)	**540–760 V**	**46–52 V**	**2 kW / 150–400 kHz**	**650 V**	**95.6 %–96.6 % @ 48 V**	**96.6 %**

* Not reported for higher voltages

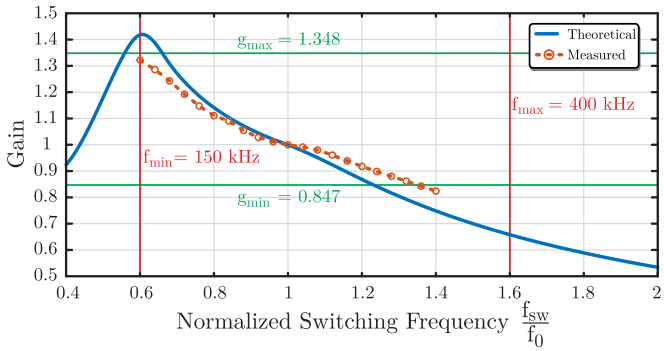

Fig. 19. Measured gain of the prototype compared to simulated gain. The green lines shows the minimum and maximum required gain and the red lines show the frequency limits of the controller.

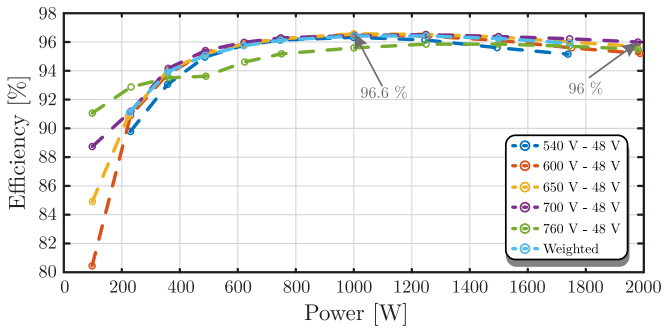

Fig. 20. Measured efficiency of the prototype for different input voltages.

the resonance frequency, and therefore the parameter deviations between the inductors and capacitors used for the resonance tank have a greater impact on the current distribution. The biggest deviations in current distribution occur at low power levels, as shown in Fig. 17(d) at 600 V and 620 W. The deviation between the currents is around 10%.

This can also be attributed to the parameter deviation of the resonance components. Throughout the entire operating range of the converter, it is evident that the most significant deviations in current distribution occur at low powers. However, at high powers, the current distribution is within a few percent. In addition, the worsening of the current distribution at lower power levels can be explained by deviations in the semiconductors and the rectifier circuit, since at very low power levels the rectification is only active on one side before the other side is also switched ON. However, since larger deviations only occur at lower power levels, the deviations in current distribution have only a minor effect on efficiency and heat distribution, as conduction losses are no longer dominant at low power levels. The even switch utilization and heat distribution is also confirmed by the thermal profile of the switches at 1.5 kW in Fig. 18. Generally, the distribution over the entire operating range deviates by no more than 6% in most cases, but can deviate by up to 10% at lower power levels. More severe current deviation can occur where the power is extremely low and the switching frequency is far from the resonance point. The employment of the multiwinding PT ensures that the current deviation is kept within reasonable limits over the entire operating and load range of the converter. Compared to a conventional litz-wire transformer, this is clearly superior, as already shown in [28].

Since the converter is connected to a HV battery, it has to cover a wide input voltage range. Therefore it is important that the converter it is able to provide the full gain range. The measured gain of the converter compared to the simulated gain is shown in Fig. 19. The curve follows the shape of the simulated curve, but shows a smaller increase below the resonance frequency than expected. In addition, the slope above the resonant frequency is less steep than expected. These deviations can be explained by the high output capacitance of the Si-MOSFETs [47] and the component tolerances and the deviation in the measurement of the magnetizing inductance of the transformer. As a result, the maximum gain is not quite reached, but this can be resolved by slightly reducing the magnetizing inductance. The less pronounced decrease above the resonant frequency can also be explained by the same reason and additionally by the parasitic capacitance of the transformer, which affects the decrease in gain above the resonant frequency, as shown

in [48]. Nevertheless, the shape of the curve correlates well with the simulation and deviations can be explained by component tolerances.

Finally, the efficiency of the system is measured. This is done by selecting different load points for different input voltages down to 48 V in closed-loop control. The efficiency of the system for these different points is presented in Fig. 20. From this, it can be seen that the efficiency curves all have a similar shape and efficiency regardless of the input voltage. This shows the effectiveness of the design approach of taking into account the electrochemistry of the battery. Achieving an evenly distributed efficiency over the entire operating range. The lowest efficiency at high power is found at an input voltage of 540 V, as conduction losses are very high at this point. In the partial load range, the lowest efficiency is recorded at 760 V, as a relatively high switching frequency is required to achieve the 48 V output voltage, because the LV switch and transformer capacitance reduces the reduction in gain. However, in general all curves from 300 to 1800 W have similar efficiencies with slight differences. The peak efficiency of 96.6% is achieved at 650 V and 1 kW power, although the converter can still achieve 96% efficiency at 2 kW and 700 V. The weighted efficiency is therefore similar to the previous curves, and most closely resembles the curve from 650 to 48 V, where most energy from the battery can be extracted.

A comparison of this work with published literature is shown in the Table IV. This highlights that most converters are optimized for the maximum or lowest input voltage and not for the voltage with the highest Q_{b}, and have a high variation of efficiency over the entire input voltage range. Demonstrating that this work achieves one of the narrowest efficiency ranges over the entire operating range and one of the highest peak efficiencies.

VI. Conclusion

In this article, a bidirectional multiwinding CLLC resonant converter with a wide and high input voltage range and distributed voltage and current stress was presented. A multiwinding CLLC topology is introduced that achieves higher peak gain compared to the standard CLLC converter, enabling higher efficiency. The topology employs two series half bridges on the HV side to distribute the voltage, opening the potential for the use of GaN semiconductors. It also has a parallel LV side to improve efficiency and heat distribution. Furthermore, a time domain analysis is presented to demonstrate the design challenges posed by the topology. A novel design procedure considering the electrochemistry of the battery for the selection of the input voltage for the transformer and for the converter parameters was proposed to achieve an optimal efficiency distribution for the varying input voltage of the battery. This is achieved by matching the input voltage of the highest efficiency of the converter to the voltage of highest differential capacity of the battery. In this context, a $\eta\rho$-pareto-optimization for the multiwinding transformer was presented and a parameter optimization for the converter was carried out, considering the rms current and the switching frequency variation, and thus the transformer and inductor losses. A prototype was built to demonstrate the effectiveness of the proposed design approach and topology. The even distribution of voltages and current in the series and parallel connection was shown, respectively. Finally, it was demonstrated that the converter achieves an evenly distributed efficiency, a peak efficiency of 96.6% and a power density of 1.36 kW/L, including protection circuits, microcontroller, and cold plate, outperforming previous solutions.

References

[1] C. Wang, P. Zheng, and J. Bauman, "A review of electric vehicle auxiliary power modules: Challenges, topologies, and future trends," *IEEE Trans. Power Electron.*, vol. 38, no. 9, pp. 11233–11244, Sep. 2023.

[2] M. Timmann and M. Renz, "48v at Mercedes-Benz–options for further applications," in *Proc. Internationales Stuttgarter Symp. Automobil-und Motorentechnik*, 2014, pp. 645–663.

[3] R. Kotb, S. Chakraborty, D.-D. Tran, E. Abramushkina, M. El Baghdadi, and O. Hegazy, "Power electronics converters for electric vehicle auxiliaries: State of the art and future trends," *Energies*, vol. 16, no. 4, Art. no. 1753.

[4] M. Di Paolo Emilio, "Electric vehicles: 48v is the new 12v," Power Electronics News, Tech. Rep. [Online]. Available: https://www.powerelectronicsnews.com/electric-vehicles-48v-is-the-new-12v/

[5] I. Aghabali, J. Bauman, P. J. Kollmeyer, Y. Wang, B. Bilgin, and A. Emadi, "800-V electric vehicle powertrains: Review and analysis of benefits, challenges, and future trends," *IEEE Trans. Transport. Electrific.*, vol. 7, no. 3, pp. 927–948, Sep. 2021.

[6] M. Buechel et al., "An automated electric vehicle prototype showing new trends in automotive architectures," in *Proc. IEEE 18th Int. Conf. Intell. Transp. Syst.*, 2015, pp. 1274–1279.

[7] C. Jung, "Power up with 800-v systems: The benefits of upgrading voltage power for battery-electric passenger vehicles," *IEEE Electrific. Mag.*, vol. 5, no. 1, pp. 53–58, Mar. 2017.

[8] B. N. Pushpakaran, A. S. Subburaj, and S. B. Bayne, "Commercial GaN-based power electronic systems: A review," *J. Electron. Mater.*, vol. 49, pp. 6247–6262, 2020.

[9] E. A. Jones, F. F. Wang, and D. Costinett, "Review of commercial GaN power devices and GaN-based converter design challenges," *IEEE J. Emerg. Sel. Topics Power Electron.*, vol. 4, no. 3, pp. 707–719, Sep. 2016.

[10] L. Shu et al., "A three-phase triple-voltage dual-active-bridge converter for medium voltage DC transformer to reduce the number of submodules," *IEEE Trans. Power Electron.*, vol. 35, no. 11, pp. 11574–11588, Nov. 2020.

[11] C. Zhao, S. D. Round, and J. W. Kolar, "An isolated three-port bidirectional DC–DC converter with decoupled power flow management," *IEEE Trans. Power Electron.*, vol. 23, no. 5, pp. 2443–2453, Sep. 2008.

[12] H. Tao, J. L. Duarte, and M. A. Hendrix, "Multiport converters for hybrid power sources," in *Proc. IEEE Power Electron. Specialists Conf.*, 2008, pp. 3412–3418.

[13] Y.-K. Tran, D. Dujić, and P. Barrade, "Multiport resonant DC-DC converter," in *Proc. 41st Annu. Conf. IEEE Ind. Electron. Soc.*, 2015, pp. 3839–3844.

[14] A. K. Bhattacharjee, N. Kutkut, and I. Batarseh, "Review of multiport converters for solar and energy storage integration," *IEEE Trans. Power Electron.*, vol. 34, no. 2, pp. 1431–1445, Feb. 2019.

[15] H. Tao, A. Kotsopoulos, J. L. Duarte, and M. A. Hendrix, "Family of multiport bidirectional DC–DC converters," *IEE Proc.-Electric Power Appl.*, vol. 153, no. 3, pp. 451–458.

[16] G. Wang, J. Mookken, J. Rice, and M. Schupbach, "Dynamic and static behavior of packaged silicon carbide MOSFETs in paralleled applications," in *Proc. IEEE Appl. Power Electron. Conf. Expo.-APEC*, 2014, pp. 1478–1483.

[17] H. Li et al., "Influence of paralleling dies and paralleling half-bridges on transient current distribution in multichip power modules," *IEEE Trans. Power Electron.*, vol. 33, no. 8, pp. 6483–6487, Aug. 2018.

[18] C. Duan, H. Bai, W. Guo, and Z. Nie, "Design of a 2.5-kW 400/12-v high-efficiency DC/DC converter using a novel synchronous rectification control for electric vehicles," *IEEE Trans. Transport. Electrific.*, vol. 1, no. 1, pp. 106–114, Jun. 2015.

[19] G. Yang, P. Dubus, and D. Sadarnac, "Double-phase high-efficiency, wide load range high-voltage/low-voltage LLC DC/DC converter for electric/hybrid vehicles," *IEEE Trans. Power Electron.*, vol. 30, no. 4, pp. 1876–1886, Apr. 2015.
[20] X. Zhou et al., "A high efficiency high power-density LLC DC-DC converter for electric vehicles (EVs) on-board low voltage DC-DC converter (LDC) application," in *Proc. IEEE Appl. Power Electron. Conf. Expo.*, 2020, pp. 1339–1346.
[21] R. Hou and A. Emadi, "A primary full-integrated active filter auxiliary power module in electrified vehicles with single-phase onboard chargers," *IEEE Trans. Power Electron.*, vol. 32, no. 11, pp. 8393–8405, Nov. 2017.
[22] M. Forouzesh and Y.-F. Liu, "Interleaved LCLC resonant converter with precise current balancing over a wide input voltage range," *IEEE Trans. Power Electron.*, vol. 36, no. 9, pp. 10330–10342, Sep. 2021.
[23] Y. Chen, H. Wang, Z. Hu, Y.-F. Liu, J. Afsharian, and Z. A. Yang, "LCLC resonant converter for hold up mode operation," in *Proc. IEEE Energy Convers. Congr. Expo.*, 2015, pp. 562–556.
[24] Y. Wei, T. Pereira, Y. Pan, M. Liserre, F. Blaabjerg, and H. A. Mantooth, "A general and automatic RMS current oriented optimal design tool for LLC resonant converters," *IEEE Trans. Emerg. Sel. Topics Power Electron.*, vol. 10, no. 6, pp. 7318–7332, Dec. 2022.
[25] R. Yu, G. K. Y. Ho, B. M. H. Pong, B. W.-K. Ling, and J. Lam, "Computer-aided design and optimization of high-efficiency LLC series resonant converter," *IEEE Trans. Power Electron.*, vol. 27, no. 7, pp. 3243–3256, Jul. 2012.
[26] T. Liu, Z. Zhou, A. Xiong, J. Zeng, and J. Ying, "A novel precise design method for LLC series resonant converter," in *Proc. 28th Int. Telecommun. Energy Conf.*, 2006, pp. 1–6.
[27] F. Groon, T. Pereira, H. Beiranvand, S. Schikowski, D. Metschies, and M. Liserre, "GaN-based multiport resonant converter for automotive applications," in *Proc. IEEE Appl. Power Electron. Conf. Expo.*, 2023, pp. 892–899.
[28] F. Groon, T. Pereira, S. Schikowski, D. Metschies, and M. Liserre, "Resonant multiport converter with high interconnection capability and lower parameter deviations," in *Proc. Europe Int. Exhib. Conf. Power Electronics, Intell. Motion, Renewable Energy Energy Manage.*, 2023, pp. 1–8.
[29] R. Wei, L. Ding, R. Liu, and Y. Li, "An intuitive and noniterative design methodology for CLLC chargers employing simplified operation modes model," *IEEE Trans. Power Electron.*, vol. 38, no. 6, pp. 7771–7784, Jun. 2023.
[30] Y. Cao, M. Ngo, D. Dong, and R. Burgos, "A simplified time-domain gain model for CLLC resonant converter," in *Proc. IEEE Energy Convers. Congr. Expo.*, 2021, pp. 3086–3079.
[31] S. De Simone, C. Adragna, C. Spini, and G. Gattavari, "Design-oriented steady-state analysis of LLC resonant converters based on FHA," in *Proc. Int. Symp. Power Electronics, Elect. Drives, Automat. Motion*, 2006, pp. 200–207.
[32] C. P. Steinmetz, "On the law of hysteresis," *Proc. IEEE*, vol. 72, no. 2, pp. 197–221, Feb. 1984.
[33] F. Groon, H. Beiranvand, T. Pereira, G. Can, and M. Liserre, "PCB layer optimization of planar medium frequency transformer for on-board EV chargers," in *Proc. 24th Eur. Conf. Power Electron. Appl. Europe*, 2022, pp. P.1–P.9.
[34] H. Beiranvand, E. Rokrok, and M. Liserre, "Vf-constrained $\eta\rho$-pareto optimisation of medium frequency transformers in ISOP-DAB converters," *IET Power Electron.*, vol. 13, no. 10, pp. 1984–1994.
[35] I. Villar, "Multiphysical characterization of medium-frequency power electronic transformers," Ph.D. dissertation, Ecole Polytechnique Fédérale de Lausanne, Lausanne, Switzerland, (n.d.). [Online]. Available: https://infoscience.epfl.ch/handle/20.500.14299/45110
[36] R. Bakri, G. Corgne, and X. Margueron, "Thermal modeling of planar magnetics: Fundamentals, review and key points," *IEEE Access*, vol. 11, pp. 41654–41679, 2023.
[37] J. Min and M. Ordonez, "Bidirectional resonant CLLC charger for wide battery voltage range: Asymmetric parameters methodology," *IEEE Trans. Power Electron.*, vol. 36, no. 6, pp. 6662–6673, Jun. 2021.
[38] H. Huang, "Designing an LLC resonant half-bridge power converter," in *Proc. Texas Instruments Power Supply Design Seminar*, Texas Instrum. Incorporated, Dallas, TX, USA, 2010, vol. 3, pp. 2010–2011.
[39] X. Xie, J. C. P. Liu, F. N. Poon, and M. H. Pong, "A novel high frequency current-driven synchronous rectifier applicable to most switching topologies," *IEEE Trans. Power Electron.*, vol. 16, no. 5, pp. 635–648, Sep. 2001.
[40] C. Zhang, Y. Jiao, Z. Shen, and P. Barbosa, "DC-link capacitor voltage balancing control for series half bridge LLC resonant converter," in *Proc. IEEE Appl. Power Electron. Conf. Expo.*, 2020, pp. 2163–2169.
[41] C. Lu, W. Hu, and F. C. Lee, "Neutral-point voltage balancing methods of series-half-bridge LLC converter for solid state transformer," *IEEE Trans. Power Electron.*, vol. 36, no. 6, pp. 7060–7073, Jun. 2021.
[42] H. van Hoek, M. Neubert, and R. W. De Doncker, "Enhanced modulation strategy for a three-phase dual active bridge—Boosting efficiency of an electric vehicle converter," *IEEE Trans. Power Electron.*, vol. 28, no. 12, pp. 5499–5507, Dec. 2013.
[43] X. Zhang, C. Yao, C. Li, L. Fu, F. Guo, and J. Wang, "A wide bandgap device-based isolated quasi-switched-capacitor DC/DC converter," IEEE transactions on power electronics, vol. 29, no. 5, pp. 2500–2510, May, 2014.
[44] D.-W. Lee, H.-S. Youn, and J.-K. Kim, "Development of phase-shift full-bridge converter with integrated winding planar two-transformer for LDC," *IEEE Trans. Transport. Electrific.*, vol. 9, no. 1, pp. 1215–1226, Mar. 2023.
[45] BorgWarner, "Gen5 high voltage DC/DC converter reference manual v1.3." [Online]. Available: https://electricdriveengineering.com.au/wp-content/uploads/2023/04/Gen5-HV-DCDC-Product-Manual.pdf
[46] Deutronic, "DVCH1503-400 gleichspannungswandler." [Online]. Available: https://www.deutronic.de/wp-content/uploads/2024/09/DVCH1503-400_db.pdf
[47] S. Ditze, T. Heckel, and M. März, "Influence of the junction capacitance of the secondary rectifier diodes on output characteristics in multi-resonant converters," in *Proc. IEEE Appl. Power Electron. Conf. Expo.*, 2016, pp. 864–871.
[48] M. A. Saket, N. Shafiei, M. Ordonez, M. Craciun, and C. Botting, "Low parasitics planar transformer for LLC resonant battery chargers," in *Proc. IEEE Appl. Power Electron. Conf. Expo.*, 2016, pp. 854–858.

Fabian Groon (Student Member, IEEE) received the B.Eng. and M.Eng. degrees in electrical engineering from the Kiel University of Applied Sciences, Kiel, Germany, in 2020 and 2021, respectively. He is currently working toward the Ph.D. degree in electrical engineering.

His research interests include dc–dc converter and planar transformers.

He is currently a Scientific Staff Member with the Chair of Power Electronics, Kiel University.

Hamzeh Beiranvand (Member, IEEE) received the B.Sc. and M.Sc. degrees in electrical engineering from Lorestan University, Khorramabad, Iran, in 2011 and 2014, respectively, and the Ph.D. degree in control strategies and efficiency optimization of solid-state transformers from Lorestan University, in 2020.

Since October 2020, he has been a Postdoctoral Researcher with the Chair of Power Electronics, Kiel University, Kiel, Germany, where he leads the Battery Systems group. He has authored more than 50 journal and conference papers. His research interests include battery system components, such as battery cell modeling and optimization, battery management systems, and power electronic converters for battery charging.

Dr. Beiranvand is a Reviewer for IEEE Power Electronics Society journals. In 2021, he was elected as a Member of the Kiel Nano, Surface, and Interface Science (KiNSIS) initiative. During his undergraduate studies, he was the recipient of a four-year scholarship by the Ministry of Education.

Dario Metschies received the B.Sc. and M.Sc. degrees in electrical engineering and information technology from Kiel University, Kiel, Germany, in 2020 and 2022, respectively.

He is currently with Reese Techware GmbH, Itzehoe, Germany, where he is involved in the design of industrial power electronics, including dc–dc converters and electric motor drives. In collaboration with Kiel University, he participated in the development of a bidirectional CLLC-resonant dc–dc converter utilizing GaN technology and planar transformers.

Sergej Schikowski received the Dipl.-Ing. degree in electrical engineering from the Kiel University of Applied Sciences, Kiel, Germany, in 2007.

He is currentlywith Reese Techware GmbH, Itzehoe, Germany, where he is developing industrial power electronics, including ac–dc and dc–dc converters as well as electric motor drive systems. In cooperation with Kiel University, he was also involved in the development of a bidirectional CLLC resonant dc–dc converter, using GaN technology and planar transformers.

Marco Liserre (Fellow, IEEE) received the M.Sc. and Ph.D. degrees in electrical engineering from the Politecnico di Bari, Bari, Italy, in 1998 and 2002, respectively.

He has been an Associate Professor with Politecnico di Bari, and since 2012, he has been a Professor of reliable power electronics with Aalborg University, Aalborg, Denmark. Since 2013, he has been a Full Professor and holds the Chair of Power Electronics at the University of Kiel, Kiel, Germany. He has been offered and declined professorships at several universities. He has authored or coauthored more than 700 technical papers (1/3 of them in international refereed journals), one book and seven granted patents (four with companies). These works have received more than 50 000 citations. From 2014 to 2021, he was selected as an Highly Cited Researcher in the field of engineering (Clarivate Web of Science). Several of his students (M.Sc., Ph.D., and post-docs) are in leading positions in industry and universities worldwide. In 2023, he joined the Fraunhofer ISIT, Itzehoe, Germany, on a part-time basis as Deputy Director and Director of the new division "Electronic Energy Systems," as well as of the Kiel branch of the Fraunhofer ISIT. From 2025, he was an Acting Director of Fraunhofer ISIT.

Dr. Liserre is a Member of IAS, PELS, PES, and IES. He has served all these societies in various capacities. In PELS, he is a Co-Editor of the IEEE OPEN ACCESS JOURNAL IN POWER ELECTRONICS and Technical Committee Chairperson of the Committee on Electronic Power Grid Systems. He has Co-Chaired several IEEE conferences being several times Chairperson. He was the recipient of 16 awards from IEEE, PCIM, and EPE-PEMC, including the prestigious 2018 IEEE-IES Mittelmann Achievement Award and the 2023 IEEE-PELS R. David Middlebrook Achievement Award. In 2023, he was the recipient of the title of "Ufficiale" by the President of the Italian Republic. In 2025, he will be Chairperson of Powertech 2025 in Kiel.